

The abundance of $z \gtrsim 10$ galaxy candidates in the HUDF using deep JWST NIRCam medium-band imaging

C. T. Donnan¹★, D. J. McLeod¹, R. J. McLure¹, J. S. Dunlop¹, A. C. Carnall¹, F. Cullen¹, D. Magee²

¹*Institute for Astronomy, University of Edinburgh, Royal Observatory, Edinburgh, EH9 3HJ, UK*

²*Department of Astronomy and Astrophysics, UCO/Lick Observatory, University of California, Santa Cruz, CA 95064, USA*

Accepted XXX. Received YYY; in original form ZZZ

ABSTRACT

We utilise *JWST* NIRCcam medium-band imaging to search for extreme redshift ($z \geq 9.5$) galaxy candidates in the Hubble Ultra Deep Field (HUDF) and the additional pointing within the GOODS-South field provided by the second NIRCcam module. Our search reveals 6 robust candidates, 3 of which have recently been spectroscopically confirmed. One of these 3 is the previously controversial $z \approx 12$ galaxy candidate UDF-22980 which is now detected in five *JWST* NIRCcam medium-band filters (F182M, F210M, F430M, F460M and F480M), efficiently excluding alternative low-redshift solutions and allowing us to now report a secure photometric redshift of $z_{\text{phot}} = 11.6 \pm 0.2$. We also detect 2 galaxies at $z \geq 12.5$ including a newly-detected candidate in the imaging provided by the second NIRCcam module (south-west of the HUDF) at $z_{\text{phot}} = 12.6 \pm 0.6$. We determine the physical properties of the 6 galaxies by fitting the 14-band photometry with BAGPIPES. We find stellar masses of $\log(M_{\star}/M_{\odot}) \approx 7.5 - 8.7$ and star-formation rates of $\log(\text{SFR}/M_{\odot}^{-1}\text{yr}^{-1}) \approx 0.3 - 5.0$. Despite the relatively small cosmological volume covered by the HUDF itself and the second NIRCcam module imaging, we find that the existence of these galaxies is fully consistent with the latest measurements of both the UV luminosity function and cosmic star-formation rate density at $z \approx 11$, supporting a gradual steady decline in the cosmic star-formation rate density out to at least $z \approx 15$.

Key words: galaxies: evolution – galaxies: formation – galaxies: high redshift

1 INTRODUCTION

The study of galaxies at the highest redshifts is crucial to unveiling the earliest stages of galaxy formation and evolution. Observations of high-redshift galaxies are vital for improving our understanding of the formation of the first stars and black holes and quantifying the role of galaxies in cosmic reionization (see Dunlop 2013 and Stark 2016 for reviews).

Until recently, the observational frontier was defined by galaxies that could be selected and studied using a combination of deep near-infrared imaging with *HST* and shallower mid-infrared imaging with *Spitzer*. This combination of facilities led to significant improvements in our understanding of galaxy evolution out to $z \approx 9$ (e.g. Ellis et al. 2013; McLure et al. 2013; Oesch et al. 2014, 2018; Finkelstein et al. 2015; McLeod et al. 2015, 2016; Bouwens et al. 2021, 2022). Due to its long-wavelength limit of $1.7 \mu\text{m}$, *HST* imaging can only identify galaxies out to $z \approx 12$, and even then only with single-band detections in the F160W filter. Prior to the launch of the *James Webb Space Telescope* (*JWST*), the most distant spectroscopically-confirmed galaxy had a redshift of $z = 10.957 \pm 0.001$: GN-z11 (Oesch et al. 2016; Jiang et al. 2021), a source that was originally selected using *HST* F160W imaging combined with non-detections at shorter wavelengths.

The landscape of high-redshift galaxy studies has now been dra-

matically changed with the advent of *JWST*, which has enabled a new era of extragalactic astronomy. The extended wavelength coverage of NIRCcam imaging to $\lambda \approx 5 \mu\text{m}$ has facilitated the robust detection of galaxies at $z \geq 10$ for the first time (e.g. Finkelstein et al. 2022b,a; Adams et al. 2023; Castellano et al. 2022; Naidu et al. 2022) including galaxy candidates at $z \approx 16$ (Donnan et al. 2023; Harikane et al. 2022). Early *JWST*-based studies of the evolving galaxy UV luminosity function imply a smooth and steady decline in the cosmic star-formation rate density (ρ_{SFRD}) out to $z \approx 15$ (Donnan et al. 2023; Harikane et al. 2022), as anticipated from some previous *HST*-based studies (e.g. McLeod et al. 2016).

Although GN-z11 was the highest redshift, spectroscopically-confirmed galaxy prior to *JWST*, another even higher-redshift galaxy candidate was identified in the *HST* UDF12 imaging of the HUDF (Ellis et al. 2013; McLure et al. 2013) with a best-fitting redshift of $z_{\text{phot}} = 11.9^{+0.3}_{-0.5}$. This galaxy (UDF12-3954-6284) is the highest-redshift candidate ever identified from *HST* imaging. In fact it was originally noted as a potential $z \approx 10$ galaxy (UDFj-39546284) from the UDF09 imaging of the HUDF (Bouwens et al. 2011), based on a F160W detection and non-detections in F125W, F105W and the HUDF ACS optical imaging. However, following the UDF12 *HST* imaging campaign, the galaxy was also found to be undetected in the F140W filter which, given the substantial overlap between the F140W and F160W filters, favoured a significantly higher redshift of $z \approx 11.9$ (Ellis et al. 2013).

Robertson et al. (2022) and Curtis-Lake et al. (2022) have recently

★ E-mail: callum.donnan@ed.ac.uk

reported *JWST* NIRCam and NIRSpect observations of 4 galaxies within the GOODS-S field from the JADES survey, including spectroscopic confirmation of UDFj-39546284 at $z_{\text{spec}} = 11.58 \pm 0.05$. They also report a galaxy at $z_{\text{spec}} = 13.20^{+0.04}_{-0.07}$ which now overtakes G_n-z11 as the highest redshift spectroscopically-confirmed galaxy. In addition, they derive stellar masses, star-formation rates and mean stellar ages for these 4 objects, finding results consistent with expectations at these redshifts.

Bouwens et al. (2022) used *JWST* NIRCam medium band imaging to measure the evolution of the UV luminosity function in the redshift range $z = 8$ -15 using high-redshift galaxy candidates selected from within the HUDF area alone. Consistent with other studies (e.g. Donnan et al. 2023; Harikane et al. 2022) their results do not support the previously suggested rapid decline in the cosmic star-formation rate density (ρ_{SFR}) beyond $z \sim 8$ (Oesch et al. 2018). However, their measurements of ρ_{SFR} at $z \gtrsim 11$ are in fact significantly higher than what was derived by Donnan et al. (2023). They also measure an absolute UV magnitude, M_{UV} , that is ≈ 1 magnitude brighter than reported by Robertson et al. (2022) for the spectroscopically confirmed $z_{\text{spec}} = 11.58 \pm 0.05$ source.

Motivated by the continued uncertainty over the nature of the UV luminosity function and cosmic star-formation rate density at $z \gtrsim 10$, we analyse a combination of the ultra-deep *HST* ACS+WFC3/IR data available in GOODS-S/UDF with the full area available from *JWST* NIRCam medium-band imaging at $\lambda \approx 2 \mu\text{m}$ and $\lambda \approx 4.5 \mu\text{m}$ to search for galaxy candidates at $z \geq 9.5$. Crucially, the new NIRCam imaging (ID 1963; PI Williams) is the first publicly available data in the HUDF red-ward of $\lambda \approx 1.6 \mu\text{m}$ with sufficient sensitivity to robustly detect candidates at $z \geq 9.5$. The aim of this study is to exploit the new *JWST* imaging data to derive secure photometric redshifts for $z \geq 9.5$ galaxy candidates and provide further constraints on the galaxy UV luminosity function and hence luminosity density at $z \geq 9.5$. We also employ Spectral Energy Distribution (SED) fitting to derive the basic properties of the stellar populations in these early galaxies.

The paper is structured as follows. In Section 2 we describe the imaging data and source catalogue creation. In Section 3 we explain the sample selection and the measurement of the physical properties of the galaxies. In Section 4 we present our derived luminosity function and the resulting inferred high-redshift dependence of the cosmic star-formation rate density. In Section 5 we discuss our results in the context of other recent observational studies and the predictions of various theoretical/numerical models of galaxy formation. Finally, in Section 6 we summarise our conclusions. Throughout we use magnitudes in the AB system (Oke 1974; Oke & Gunn 1983), and assume a standard cosmological model with $H_0 = 70 \text{ km s}^{-1} \text{ Mpc}^{-1}$, $\Omega_m = 0.3$ and $\Omega_\Lambda = 0.7$.

2 DATA

2.1 Imaging

We utilise deep imaging from *HST* and *JWST* in the HUDF. From *HST* we use data covering the wavelength range $\lambda \approx 0.4 - 1.6 \mu\text{m}$ from ACS F435W, F606W, F775W, F814W, F850LP and WFC3 F105W, F125W, F140W and F160W imaging. We utilise new *JWST* imaging from the HUDF medium-band survey (ID 1963; PI Williams) which contains deep NIRCam imaging through the F182M, F210M, F430M, F460M and F480M filters (Williams et al. 2023). The 5σ global depths for F182M and F210M are $m_{\text{AB}} \approx 29$ and for F430M, F460M and F480M they are $m_{\text{AB}} \approx 28.5$. The data

were reduced using the Primer Enhanced NIRCam Image Processing Library (PENCIL; Magee et al., in prep) software, a customised version of the *JWST* pipeline v1.8.0. The CRDS context used was “jwst_1011.pmap”, which includes the most recent NIRCam zero-point corrections and in-flight calibrations. An extended description is available in Donnan et al. (2023).

2.2 Catalogue creation and photometry

We perform a search for galaxies using SExtractor (Bertin & Arnouts 1996) in dual-image mode. We use the F182M band image as the detection image as it is the deepest imaging sampling flux long-ward of the Lyman break. For the photometry in the *JWST* NIRCam imaging, we use a similar technique to Donnan et al. (2023), with 0.24 arcsec-diameter apertures in the SW filters (F182M, F210M) and 0.3 arcsec-diameter apertures in the LW filters (F430M, F460M, F480M). We also use 0.3 arcsec-diameter apertures in the *HST* ACS and WFC3 filters. All of the photometry was then corrected to 76% of total (as this is approximately the flux enclosed by the apertures utilised for F182M) using a point-source correction based on the curve-of-growth of each filter’s PSF. We adopt the 1σ local depth as the error on the fluxes measured through each filter. This was determined by $1.483 \times \text{MAD}$ where MAD is the median absolute deviation of the flux in the closest 200 empty apertures to the source.

3 GALAXY SAMPLE

3.1 Sample selection

We use the photometric redshift (photo- z) code EAZY (Brammer et al. 2008) for our primary redshift determination, fitting with the PEGASE (Fioc & Rocca-Volmerange 1999) set of templates which include nebular emission lines. We determine the primary solution by allowing templates to vary over the redshift range $0 < z < 25$ and a secondary low-redshift solution by restricting the redshift range to $0 < z < 6$. We select our sample by requiring a best-fitting photometric redshift at $z \geq 9.5$ with a threshold value of $\Delta\chi^2 \geq 4$ between the primary and secondary solution. Due to the position of the Lyman break, we require the flux to be $< 2\sigma$ in all the ACS filters. We also require the flux to be $> 5\sigma$ in either F160W or F182M with the next reddest filter at 3σ to ensure a robust detection long-ward of the Lyman break. We visually inspect the final sample to remove artefacts and diffraction spikes. To verify the robustness of the photometric redshifts, we also fitted the photometry using two further SED fitting codes: LePhare (Arnouts et al. 1999; Ilbert et al. 2006) with templates from Bruzual & Charlot (2003) and with dust attenuation spanning the range $A_V = 0.0 - 6.0$, and also the code described in McLure et al. (2011). We require all candidates in the final sample to have significantly preferred high-redshift solutions from all three codes.

3.2 Final sample

The final sample contains 6 galaxies at $z \geq 9.5$. The measured photometry, corrected to total, is listed in Table 1 and the photometric redshifts of the galaxy candidates are listed in Table 2. Out of these 6 sources, one is UDFj-39546284 (UDF-22980 in this study) which is the previously-detected source at $z \approx 12$ (e.g. Bouwens et al. 2011; Ellis et al. 2013) with recent spectroscopic confirmation at $z_{\text{spec}} = 11.58$ (Curtis-Lake et al. 2022). Our best-fitting photo- z for this galaxy from EAZY is in excellent agreement with this, yielding

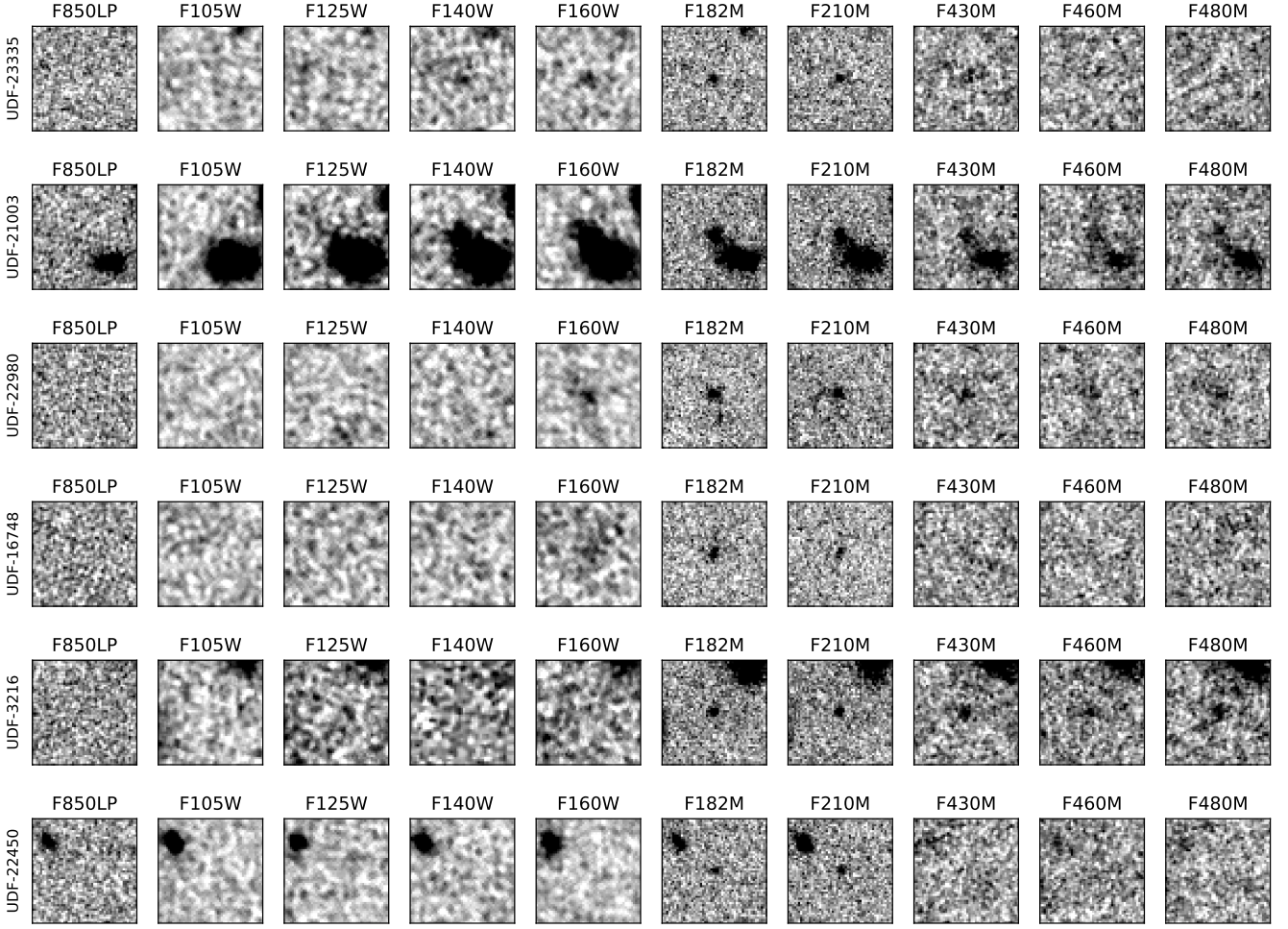


Figure 1. Postage-stamp greyscale images of the six $z \gtrsim 9.5$ galaxy candidates from our sample in the *HST* and *JWST* imaging. The imaging is ordered by increasing wavelength from left to right. Each postage-stamp image is 1.5×1.5 arcsec in size, with North to the top and East to the left.

Table 1. The observed photometry for the galaxies in the *JWST*-selected sample in AB magnitudes. The first column lists the ID of the object. The following columns show the photometry in each of the relevant ACS, WFC3 and NIRCcam filters. In the case of a non-detection at the 2σ level the photometry is shown as an upper limit.

ID	F850LP	F105W	F125W	F140W	F160W	F182M	F210M	F430M	F460M	F480M
23335	>30.40	>31.20	$30.49^{+0.45}_{-0.32}$	$29.71^{+0.18}_{-0.15}$	$29.41^{+0.14}_{-0.12}$	$28.94^{+0.14}_{-0.13}$	$29.10^{+0.21}_{-0.18}$	$28.85^{+0.41}_{-0.3}$	>28.95	>29.25
21003	>30.41	$30.68^{+0.36}_{-0.27}$	$29.27^{+0.12}_{-0.1}$	$28.09^{+0.06}_{-0.05}$	$27.77^{+0.06}_{-0.05}$	$27.84^{+0.06}_{-0.05}$	$27.94^{+0.06}_{-0.05}$	$28.00^{+0.2}_{-0.17}$	$27.89^{+0.21}_{-0.17}$	$28.26^{+0.22}_{-0.18}$
22980	>30.48	>31.37	>31.00	>30.93	$29.04^{+0.1}_{-0.09}$	$28.33^{+0.09}_{-0.08}$	$28.32^{+0.08}_{-0.08}$	$28.37^{+0.2}_{-0.17}$	$28.02^{+0.19}_{-0.17}$	$28.21^{+0.23}_{-0.19}$
16748	>30.16	>30.93	>30.50	>30.54	$29.68^{+0.29}_{-0.23}$	$28.93^{+0.18}_{-0.15}$	$29.10^{+0.4}_{-0.29}$	$29.15^{+0.62}_{-0.39}$	>29.24	$29.24^{+0.67}_{-0.41}$
3216	>28.87	>29.69	>29.49	>28.03	>29.22	$28.69^{+0.1}_{-0.09}$	$28.75^{+0.13}_{-0.11}$	$28.33^{+0.23}_{-0.19}$	$28.30^{+0.25}_{-0.21}$	$28.39^{+0.15}_{-0.13}$
22450	>30.28	>31.39	>30.69	>30.99	>31.01	$29.29^{+0.19}_{-0.16}$	$28.99^{+0.22}_{-0.18}$	>29.16	>29.20	>29.26

$z = 11.65^{+0.17}_{-0.21}$, with a $\Delta\chi^2 = 40$ between the primary solution and the low-redshift secondary solution ($z = 2.9^{+0.1}_{-0.1}$), indicating a clear preference for the primary (higher) redshift. This is consistent with the photo- z from (Ellis et al. 2013; McLure et al. 2013) which at the time was based on only a F160W detection (combined with non-detections through other *HST* and *Spitzer* filters).

UDF-21003, with a photo- z of $z = 9.8^{+0.2}_{-0.1}$, is a newly-detected

source which is in fact the most robustly detected candidate in the sample. It was previously undetected likely due to the close positioning of a low-redshift nearby source. UDF-3216 is newly-detected candidate at $z = 12.6 \pm 0.7$ which is located in the second/parallel NIRCcam module. Multi-wavelength postage-stamp images of the 6 galaxies in the sample are shown in Fig. 1, while the photometric

data for the sample along with the two alternative (high-redshift and low-redshift) SED fits for each galaxy are shown in Fig. 2.

Robertson et al. (2022) reported photometric properties of 4 galaxies with spectroscopic confirmation in a companion paper (Curtis-Lake et al. 2022) using data from the JADES survey. We recover 3 of the 4 galaxies in their sample (the fourth source is positioned outside the medium band imaging) with our photometric redshifts broadly consistent with their spectroscopic redshifts. These are noted in the final column in Table 2.

Bouwens et al. (2022) also recently searched for galaxies using the JWST UDF medium band survey and found 4 galaxies at $z \geq 9.5$. We recover 3 of these candidates in our sample as indicated in Table 2. The 4th source, XDFH-2334046578 in Bouwens et al. (2022), is not included in this sample as it failed the visual inspection stage due to an unusual positional offset of the source in F160W. Therefore we were not confident in the strength of the break between the F160W and F182M filters. For the 3 we recover, we find good agreement overall in the photometric redshifts. However, for UDF-22980 we measure a moderately lower redshift. We also find a significantly fainter absolute UV magnitude for this source of $M_{UV} = -19.4$ compared to the value of $M_{UV} = -20.2$ reported by Bouwens et al. (2022). Our value of M_{UV} is in close agreement to that given by Robertson et al. (2022) which exploits the additional constraints provided by the broadband NIRCам imaging in the JADES survey.

Our sample contains 2 galaxy candidates at $z > 12.5$, UDF-3216 and UDF-22450 which have best fitting redshifts of $z = 12.6^{+0.6}_{-0.7}$ and $z = 13.5^{+0.3}_{-0.8}$ respectively. Despite the photometric redshift relying on detections in only 2 filters, our photometric redshift measurement of UDF-22450 is in close agreement with the spectroscopic redshift of $z_{\text{spec}} = 13.20$ recently reported by Robertson et al. (2022).

3.3 Physical properties

All the fluxes were corrected to total assuming a point source correction based on the curve-of-growth. We then use the BAGPIPES spectral fitting code (Carnall et al. 2018) to further constrain the physical properties of the galaxies in our sample. We run BAGPIPES using the configuration described in Carnall et al. (2020, 2023), which includes the 2016 updated version of the Bruzual & Charlot (2003) stellar population models with the MILES stellar spectral library, an emission line prescription calculated using the Cloudy photoionization code (Ferland et al. 2017), the Salim et al. (2018) dust attenuation model and a constant SFH model. The recovered stellar masses and mass-weighted mean stellar ages for all 6 galaxies are noted in Table 2. We find that these galaxies have relatively low stellar masses ($\log(M_*/M_\odot) \approx 7.5 - 8.7$) and star-formation rates in the range $\log(\text{SFR}/M_\odot\text{yr}^{-1}) \approx 0.3 - 5.0$. The limited detections longward of the Balmer break prevent any conclusive constraints on the stellar ages of these galaxies. Nevertheless, the mean stellar ages derived from BAGPIPES are moderate (~ 40 Myr), and for those with spectroscopic confirmation, are consistent with ages derived using the more extensive filter coverage in the JADES survey (Robertson et al. 2022).

Using the filters long-ward of the Lyman break we determine the rest-frame UV continuum slope, β (where flux $f_\lambda \propto \lambda^\beta$) with the technique described in Cullen et al. (2023). Due to the limited number of filters beyond the Lyman break, the UV slope remains relatively unconstrained for most of these objects. However, we measure a robust UV slope for UDF-21003, finding $\beta = -2.5 \pm 0.2$. This represents a very blue UV continuum indicating the presence of a young, low-metallicity stellar population. However, we note that

Cullen et al. (2023) found a median UV slope of $\beta = -2.29 \pm 0.09$ at $8 < z < 16$, indicating that UDF-21003 is fully consistent with the average UV slope found at these redshifts.

4 LUMINOSITY FUNCTION

We compute the UV luminosity function at $z \approx 11.2$ using objects detected at 8σ in F182M in a redshift bin spanning $9.5 \leq z \leq 13.5$ (with the upper redshift limit set by the fact the Lyman break cuts into the F182M filter at $z \approx 13.5$). Four galaxies are selected using this condition which are contained within a bin centred at $M_{UV} = -19.2$ with a width of 1 magnitude. The use of a redshift bin spanning $\Delta z = 4$ reduces the impact of photo- z uncertainties on our derivation of the LF.

The binned co-moving number density of sources per absolute magnitude, $\Phi(M_{UV})$, is determined using the $1/V_{\text{max}}$ method (Schmidt 1968). The volume, V_{max} , is defined as the difference in co-moving volume between the volume at $z = 9.5$ and the maximum redshift that the galaxy could be detected at 8σ in F182M with a limit at $z = 13.5$ for this selection. We find that 2 of the sources are detectable to $z = 13.5$ whereas the 2 fainter sources are only detectable to $z \approx 11.8$ and $z \approx 12.6$. Therefore the average redshift of the limited volumes is $z \approx 11.2$. In order to account for incompleteness in the galaxy sample, we perform completeness simulations using the same method as described in Donnan et al. (2023), with point sources injected into the F182M imaging in 3 regions across the 2 modules. From $m_{\text{AB}} = 24-31$ in steps of 0.1, 800 sources are injected into each region and the rate of recovery measured. This process is repeated 10 times for each region which therefore results in a total of 1,680,000 sources injected into the imaging. This generates the completeness as a function of apparent magnitude in the detection image, F182M.

As the UV LF is derived here using a relatively small cosmological volume (Donnan et al. (2023) use a $\sim 5\times$ larger volume), our results are more vulnerable to cosmic variance. To account for this we use the cosmic variance calculator from Trenti & Stiavelli (2008). We measure an uncertainty of 27% due to cosmic variance which is smaller than the uncertainties arising from the small sample size. The cosmic variance uncertainty was factored into the final uncertainty on the number density. The resultant galaxy number density in this bin is shown in Fig. 3 where $\Phi(M_{UV} = -19.2) = (1.03^{+0.86}_{-0.57}) \times 10^{-4} \text{ mag}^{-1} \text{ Mpc}^{-3}$.

This new estimate at $z \approx 11.2$ is fully consistent with the recently-reported evolution of the UV LF from $z \sim 10.5$ to $z \sim 13.25$ (Donnan et al. 2023). We fit a double-power law (DPL) using the same technique described in Donnan et al. (2023) where we fix α , β and M_* to -2.10 , -3.53 , -19.12 respectively. These are the best fitting values at $z \sim 10.5$ (Donnan et al. 2023) and therefore we allow only ϕ_* as a free parameter. This results in a best-fitting DPL model with $\phi_* = (2.36 \pm 1.60) \times 10^{-4}/\text{mag}/\text{Mpc}^3$. We then perform a luminosity-weighted integral of the best-fitting DPL model to derive the comoving UV luminosity density (ρ_{UV}) and therefore cosmic star-formation rate density (ρ_{SFR}). This is shown as the red point in Fig. 4 which is in good agreement with the log-linear relation from Donnan et al. (2023, solid black line) and is therefore consistent with a steady, exponential decline in ρ_{UV} to $z \sim 15$. Our results are inconsistent with the result at $z \sim 12.6$ from Bouwens et al. (2022) as they predict a significantly higher ρ_{UV} as shown by the green point at $z \sim 12.6$ in Fig. 4. This is possibly impacted by their estimate of M_{UV} for UDF-22980 which is ~ 0.8 mag brighter than derived here (see Section 3.2). They also restrict their search to the HUDF area alone and therefore probe a smaller cosmological volume than utilised in

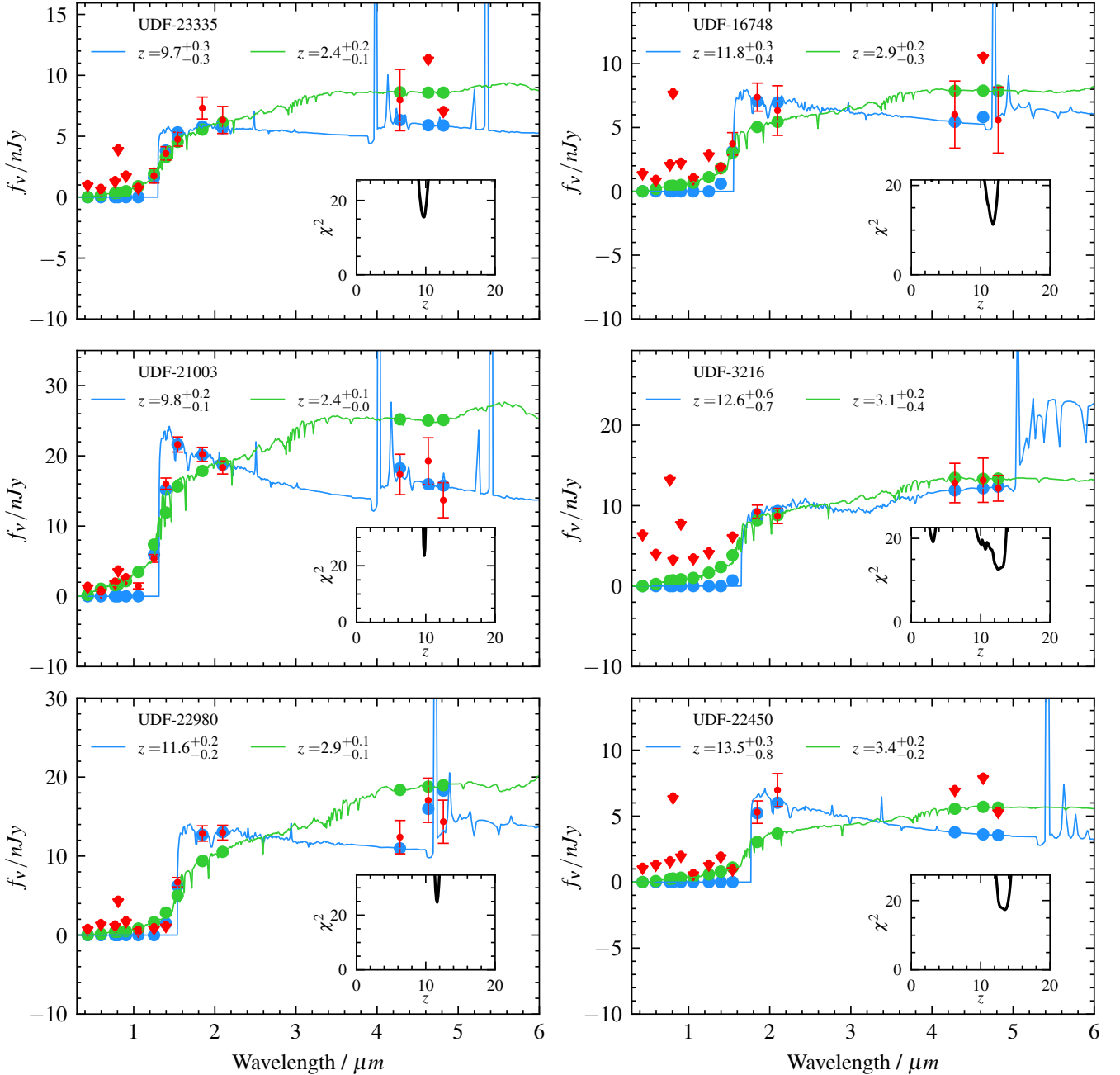


Figure 2. Alternative Spectral Energy Distribution (SED) fits for the six $z \geq 9.5$ galaxies in the sample. The blue line shows the best-fitting (preferred) high-redshift solution, the green line shows the best-fitting (alternative) low-redshift solution, and the red points show the measured photometry (at 76% of total flux). The red arrows show upper limits in the case of a non-detection at the 2σ level. The solid blue and green circles represent the model photometry of the best-fitting high and low-redshift templates respectively. The value of χ^2 as a function of redshift is shown for each source in the inset panel.

this search, which, as they mention, also makes their measurement of the UV LF somewhat more sensitive to cosmic variance. They report a cosmic variance uncertainty of $\sim 52\%$ using the [Trenti & Stiavelli \(2008\)](#) calculator which is notably larger than we calculate for our LF ($\sim 27\%$). [Bouwens et al. \(2022\)](#) also use a significantly steeper value of the faint end slope of $\alpha = -2.71$. As ρ_{UV} is particularly sensitive to α , their steeper faint-end slope also contributes to this increased value of ρ_{UV} .

5 DISCUSSION

5.1 The growth of early galaxies

The early-release NIRCcam data demonstrated the ability of *JWST* to detect numerous galaxies at $z > 9$ (e.g. [Adams et al. 2023](#); [Castellano et al. 2022](#); [Naidu et al. 2022](#); [Finkelstein et al. 2022b](#)) including a detection of a galaxy candidate at $z \approx 16$ ([Donnan et al. 2023](#)) which has since been verified by multiple studies (e.g. [Harikane et al. 2022](#); [Finkelstein et al. 2022a](#)). This indicates that galaxy formation

Table 2. The best-fitting photometric redshifts and derived physical properties of the six $z \geq 9.5$ galaxy candidates. The first column shows the ID of the object followed by the best-fitting photometric redshift from EAZY. The following columns show the UV slope (β), stellar mass, star-formation rate and mean stellar age from BAGPIPES, the absolute UV magnitude and the coordinates of each object. The penultimate column notes if the source was also reported by Bouwens et al. (2022) and the final column shows, where available, the spectroscopic redshift from Curtis-Lake et al. (2022).

ID	z_{phot}	β	$\log(M_{\star}/M_{\odot})$	$\log(\text{SFR}/M_{\odot}/\text{yr})$	t_{\star}/Myr	M_{UV}	RA	Dec	B22	z_{spec}
23335	$9.68^{+0.28}_{-0.28}$	-0.8 ± 0.6	$7.5^{+0.4}_{-0.2}$	$0.3^{+0.5}_{-0.1}$	7^{+38}_{-5}	-18.13	03:32:38.12	-27:46:24.56	Yes	10.38
21003	$9.79^{+0.15}_{-0.13}$	-2.5 ± 0.2	$8.1^{+0.2}_{-0.3}$	$1.3^{+1.0}_{-0.7}$	34^{+48}_{-25}	-19.63	03:32:42.13	-27:46:50.28	-	-
22980	$11.65^{+0.17}_{-0.21}$	-2.3 ± 0.5	$8.3^{+0.4}_{-0.6}$	$2.4^{+2.5}_{-1.9}$	44^{+104}_{-36}	-19.36	03:32:39.55	-27:46:28.62	Yes	11.58
16748	$11.77^{+0.29}_{-0.44}$	-3.3 ± 1.6	$7.9^{+0.4}_{-0.5}$	$0.8^{+0.9}_{-0.6}$	41^{+115}_{-33}	-18.71	03:32:40.47	-27:47:33.93	Yes	-
3216	$12.56^{+0.64}_{-0.66}$	-2.4 ± 1.1	$8.7^{+0.4}_{-0.7}$	$5.0^{+7.8}_{-3.9}$	40^{+107}_{-31}	-19.13	03:32:29.20	-27:49:48.46	-	-
22450	$13.54^{+0.28}_{-0.76}$	-1.6 ± 2.1	$7.8^{+0.4}_{-0.5}$	$0.7^{+0.6}_{-0.5}$	52^{+87}_{-39}	-18.73	03:32:35.97	-27:46:35.39	-	13.20

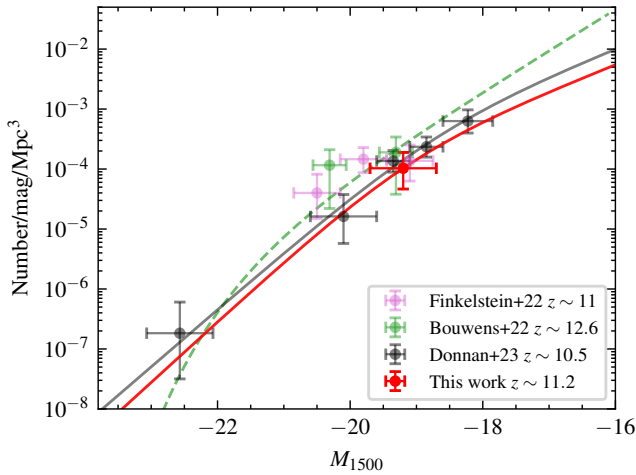


Figure 3. The UV luminosity function (LF) determined from our new sample in the redshift range $9.5 < z < 13.5$ (red point). The rest-frame UV LF at $9.5 < z < 11.5$ from Donnan et al. (2023) is shown as black points with the best-fitting double power-law shown as a solid black line. We include data points from Finkelstein et al. (2022a) and Bouwens et al. (2022), with the best-fitting Schechter function from Bouwens et al. (2022) plotted as the dashed green line. The derived number density based on our new $9.5 < z < 13.5$ galaxy sample is clearly consistent with the evolution of the UV LF derived by Donnan et al. (2023).

commenced at $z > 16$ and therefore within < 250 Myr of the big bang. The results from this new study give further support to this conclusion with the detection of 6 galaxies at $9.5 < z \lesssim 13.5$ from within a relatively small cosmological volume. As demonstrated in this analysis, this corresponds to a number density consistent with the evolution of the UV LF derived by Donnan et al. (2023). This leads to a value of the UV luminosity density (and cosmic star-formation rate density) at $z \approx 11.5$ which is fully consistent with the log-linear relation derived in Donnan et al. (2023) of:

$$\log_{10}(\rho_{\text{UV}}) = (-0.231 \pm 0.037)z + (27.5 \pm 0.3). \quad (1)$$

The results of this study thus further support the analytical prediction from Hernquist & Springel (2003) that a steady, exponential decline in ρ_{SFR} is expected with increasing redshift, as illustrated by the solid line in the left-hand panel of Fig. 4. In the right-hand panel of Fig. 4 we additionally provide a comparison of the new observational constraints on the UV luminosity density with the pre-

dictions of various different theoretical/numerical models. Although the observational data points lie below the extreme-redshift extrapolation of the relation provided by Madau & Dickinson (2014), they sit above the predictions from semi-empirical constant star-formation efficiency models as deduced by Mason et al. (2022) and Tacchella et al. (2018). We also compare to the cosmological hydrodynamical simulations FiBY (Johnson et al. 2013; Paardekooper et al. 2015), FLARES (Wilkins et al. 2022) and MilleniumTNG (Kannan et al. 2022). Overall, it can be seen that there is a wide range in the predictions of the different theoretical models; the new observational constraints sit above most of the theoretical curves but are reasonably in-line with the predictions from FLARES and the semi-analytical model presented by Behroozi & Silk (2015).

5.2 Low-redshift solutions for the $z \approx 12$ candidate

After UDF-22980 was proposed to lie at $z = 11.9$ (Ellis et al. 2013; McLure et al. 2013), there followed much discussion on the nature of this object, in part informed by a series of follow-up observations. Brammer et al. (2013) used *HST* GRISM spectroscopy and Capak et al. (2013) used Keck MOSFIRE to search for emission lines. No robust emission lines were detected but tentative ($\sim 2\sigma$) detections were reported at $\lambda_{\text{obs}} \approx 1.6\mu\text{m}$. It was concluded that this could be consistent with an [OIII] $\lambda 4959, 5007$ detection at $z = 2.19$ or [OII] $\lambda 3727, 3729$ at $z = 3.29$. Now, however, with the *JWST* medium band imaging at $\lambda_{\text{obs}} > 1.6\mu\text{m}$ we can robustly constrain the shape of the galaxy SED. We find that, fitting with EAZY and LePhare, the new enhanced photometry is inconsistent with any solution at $z = 2.19$ or $z = 3.29$. When the fit is forced to these redshifts we find that the best-fitting (formally unacceptable) solution is an old passive galaxy which would not have the strong emission lines required for these low- z solutions. Another inconsistency with the low- z solution is that a strong [OIII] emitter at $z = 2.19$ would likely have strong H α emission at $\lambda_{\text{obs}} = 2.1\mu\text{m}$. This would result in a substantially smaller flux in F182M than in F210M which is not what is observed. This conclusion is also reinforced by the recent *JWST* spectroscopic observations from the JADES survey, albeit no emission lines were detected with NIRSspec (Robertson et al. 2022; Curtis-Lake et al. 2022).

5.3 The power of medium-band imaging

Accurate spectroscopic confirmation of $z \geq 7$ galaxies at optical/near-infrared wavelengths has been, and indeed continues to be a challenge due to the attenuation of Ly α emission within the epoch of

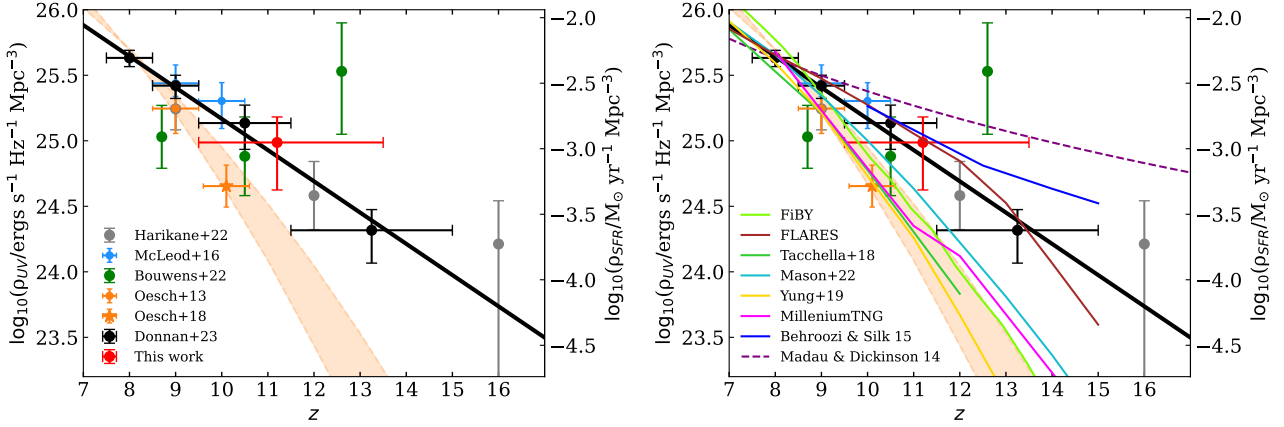


Figure 4. The redshift evolution of the UV luminosity density, ρ_{UV} , and hence the inferred cosmic star-formation rate density, ρ_{SFR} , at $z > 7$ with our new measurement at $z \sim 11.2$ (red circular data point). Estimates at $z \approx 9 - 10$ from Oesch et al. (2013, 2018) and McLeod et al. (2016) are shown by the orange and blue data points respectively. The green and grey points show ρ_{UV} derived from the LFs in Bouwens et al. (2022) and Harikane et al. (2022) respectively. All values were determined using a limit of $M_{UV} = -17$ in the luminosity-weighted integral. The black data points and solid line show the results from Donnan et al. (2023). The shaded orange region shows the halo evolution model from Oesch et al. (2018). The right-hand panel shows a comparison to theoretical models, again setting the LF integration limit to $M_{UV} = -17$. The green, cyan, blue and yellow lines show semi-analytic models from Tacchella et al. (2018), Mason et al. (2022), Behroozi & Silk (2015) and Yung et al. (2019) respectively. The green, brown and pink lines show the results of hydrodynamical simulations from FiBY (Johnson et al. 2013; Paardekooper et al. 2015), FLARES (Wilkins et al. 2022) and MilleniumTNG (Kannan et al. 2022). The dashed purple line shows an extrapolation at $z \geq 8$ of the $\rho_{UV} \propto (1+z)^{-2.9}$ relation from Madau & Dickinson (2014). Our new measurement is fully consistent with the steady, exponential decline in ρ_{UV} up to $z \approx 15$ described in Donnan et al. (2023).

reionization. An alternative route to robust spectroscopic redshifts is provided by the Atacama Large Millimeter/submillimeter Array (ALMA), with spectroscopic redshifts of $z \geq 7$ galaxies now regularly secured at sub-mm wavelengths. For example, ALMA has now been used to confirm galaxies at $z = 9.1$ (Hashimoto et al. 2018) and $z = 8.38$ (Laporte et al. 2017) based on the detection of [OIII] at $\lambda_{rest} = 88 \mu\text{m}$ as well as observations of [CII] at $\lambda_{rest} = 158 \mu\text{m}$. As the required observation time with ALMA is strongly dependent on the confidence interval of the photometric redshift (due to the potential requirement for multiple tunings), robust photometric redshifts are required for efficient sub-mm/mm spectroscopic confirmation. The results presented here thus demonstrate that *JWST* NIRCcam medium-band imaging can be an invaluable additional tool for refining the photometric redshifts of high-redshift galaxy candidates in preparation for ALMA follow-up spectroscopy.

6 CONCLUSIONS

We have used a combination of the deepest optical + near-infrared *HST* broad-band imaging with deep *JWST* NIRCcam medium-band imaging to detect 6 galaxy candidates at $z \geq 9.5$.

We obtain a robust photometric redshift for 6 candidates including the previously reported $z \approx 12$ galaxy candidate, UDF-22980, at $z_{phot} \approx 11.6$. We find that the previously suggested low- z emission line galaxy solutions indicated from $\sim 2\sigma$ spectroscopic detections at $\lambda_{obs} = 1.6 \mu\text{m}$ are incompatible with the *JWST* NIRCcam photometry which instead re-affirms the $z \approx 12$ solution and refines the photometric redshift to $z = 11.65^{+0.17}_{-0.21}$. The robustness of the solutions were tested using 4 independent SED fitting codes which all show good agreement.

We also report UV slopes, stellar masses, star-formation rates and mass-weighted mean stellar ages for all 6 candidates. We find stellar

masses of $\log(M_{\star}/M_{\odot}) \approx 7.5 - 8.7$ and star-formation rates of $\log(\text{SFR}/M_{\odot}\text{yr}^{-1}) \approx 0.3 - 5.0$. We are able to measure a robust UV continuum slope for one object, finding a very blue slope of $\beta = -2.5 \pm 0.2$ which is consistent with a young, low-metallicity stellar population.

The galaxy number density and hence cosmic star-formation rate density at $z \approx 11$ derived from this sample are fully consistent with the current picture of the evolution of the UV LF with a gradual steady decline over the redshift range $z = 8-15$. The resulting inferred gradual (exponential) decline in cosmic star-formation rate density out to at least $z \approx 15$ is clearly inconsistent with at least some theoretical/numerical models of early galaxy evolution.

This study further demonstrates the power of *JWST* to quickly reveal the true nature of $z \geq 10$ candidates that were first identified by *HST* as well as to detect new galaxy candidates, with the NIRCcam medium-band imaging analysed here providing sensitive photometry at $\lambda_{obs} \gtrsim 1.6 \mu\text{m}$. Robust photometric redshifts are vital for drawing conclusions about the physical properties of $z \geq 10$ galaxies as well as providing a tighter frequency range for ALMA follow-up spectroscopy. Forthcoming *JWST* surveys will primarily target fields that are accessible to ALMA, and were heavily imaged by *HST* such as NGDEEP (GO 2079) and PRIMER (GO 1837)¹ and will therefore benefit from this combination. Therefore, it is likely these surveys will provide large statistically-significant samples of galaxies over a wide redshift range which will yield further constraints on the high-redshift evolution of the UV luminosity function as well as providing numerous extreme-redshift galaxy candidates for follow-up *JWST* and ALMA spectroscopy.

¹ <https://primer-jwst.github.io/>

ACKNOWLEDGEMENTS

We thank the referee Richard S. Ellis for useful comments which helped improve the quality of the manuscript. We are grateful to Stephen Wilkins and Andrea Incatasciato for providing simulation data. C. T. Donnan, D. J. McLeod, R. J. McLure, J. S. Dunlop acknowledge the support of the Science and Technology Facilities Council. A.C. Carnall thanks the Leverhulme Trust for their support via the Leverhulme Early Career Fellowship scheme. F. Cullen acknowledges support from a UKRI Frontier Research Guarantee Grant [grant reference EP/X021025/1]. For the purpose of open access, the author has applied a Creative Commons Attribution (CC BY) licence to any Author Accepted Manuscript version arising from this submission.

DATA AVAILABILITY

The inclusion of a Data Availability Statement is a requirement for articles published in MNRAS. Data Availability Statements provide a standardised format for readers to understand the availability of data underlying the research results described in the article. The statement may refer to original data generated in the course of the study or to third-party data analysed in the article. The statement should describe and provide means of access, where possible, by linking to the data or providing the required accession numbers for the relevant databases or DOIs.

REFERENCES

- Adams N. J., et al., 2023, *MNRAS*, **518**, 4755
 Arnouts S., Cristiani S., Moscardini L., Matarrese S., Lucchin F., Fontana A., Giallongo E., 1999, *MNRAS*, **310**, 540
 Behroozi P. S., Silk J., 2015, *ApJ*, **799**, 32
 Bertin E., Arnouts S., 1996, *A&AS*, **117**, 393
 Bouwens R. J., et al., 2011, *Nature*, **469**, 504
 Bouwens R. J., et al., 2021, *AJ*, **162**, 47
 Bouwens R. J., et al., 2022, *arXiv e-prints*, p. [arXiv:2211.02607](https://arxiv.org/abs/2211.02607)
 Brammer G. B., van Dokkum P. G., Coppi P., 2008, *ApJ*, **686**, 1503
 Brammer G. B., van Dokkum P. G., Illingworth G. D., Bouwens R. J., Labbé I., Franx M., Momcheva I., Oesch P. A., 2013, *ApJ*, **765**, L2
 Bruzual G., Charlot S., 2003, *MNRAS*, **344**, 1000
 Capak P., Faisst A., Vieira J. D., Tacchella S., Carollo M., Scoville N. Z., 2013, *ApJ*, **773**, L14
 Carnall A. C., McLure R. J., Dunlop J. S., Davé R., 2018, *MNRAS*, **480**, 4379
 Carnall A. C., et al., 2020, *MNRAS*, **496**, 695
 Carnall A. C., et al., 2023, *MNRAS*, **518**, L45
 Castellano M., et al., 2022, *ApJ*, **938**, L15
 Cullen F., et al., 2023, *MNRAS*, **520**, 14
 Curtis-Lake E., et al., 2022, *arXiv e-prints*, p. [arXiv:2212.04568](https://arxiv.org/abs/2212.04568)
 Donnan C. T., et al., 2023, *MNRAS*, **518**, 6011
 Dunlop J. S., 2013, in Wiklind T., Mobasher B., Bromm V., eds, *Astrophysics and Space Science Library* Vol. 396, *The First Galaxies*. p. 223 ([arXiv:1205.1543](https://arxiv.org/abs/1205.1543)), [doi:10.1007/978-3-642-32362-1_5](https://doi.org/10.1007/978-3-642-32362-1_5)
 Ellis R. S., et al., 2013, *ApJ*, **763**, L7
 Ferland G. J., et al., 2017, *Rev. Mex. Astron. Astrofis.*, **53**, 385
 Finkelstein S. L., et al., 2015, *ApJ*, **810**, 71
 Finkelstein S. L., et al., 2022a, *arXiv e-prints*, p. [arXiv:2211.05792](https://arxiv.org/abs/2211.05792)
 Finkelstein S. L., et al., 2022b, *ApJ*, **940**, L55
 Fioc M., Rocca-Volmerange B., 1999, *arXiv e-prints*, pp [astro-ph/9912179](https://arxiv.org/abs/astro-ph/9912179)
 Harikane Y., et al., 2022, *arXiv e-prints*, p. [arXiv:2208.01612](https://arxiv.org/abs/2208.01612)
 Hashimoto T., et al., 2018, *Nature*, **557**, 392
 Hernquist L., Springel V., 2003, *MNRAS*, **341**, 1253
 Ilbert O., et al., 2006, *A&A*, **457**, 841

- Jiang L., et al., 2021, *Nature Astronomy*, **5**, 256
 Johnson J. L., Dalla Vecchia C., Khochfar S., 2013, *MNRAS*, **428**, 1857
 Kannan R., et al., 2022, *arXiv e-prints*, p. [arXiv:2210.10066](https://arxiv.org/abs/2210.10066)
 Laporte N., et al., 2017, *ApJ*, **837**, L21
 Madau P., Dickinson M., 2014, *ARA&A*, **52**, 415
 Mason C. A., Trenti M., Treu T., 2022, *arXiv e-prints*, p. [arXiv:2207.14808](https://arxiv.org/abs/2207.14808)
 McLeod D. J., McLure R. J., Dunlop J. S., Robertson B. E., Ellis R. S., Targett T. A., 2015, *MNRAS*, **450**, 3032
 McLeod D. J., McLure R. J., Dunlop J. S., 2016, *MNRAS*, **459**, 3812
 McLure R. J., et al., 2011, *MNRAS*, **418**, 2074
 McLure R. J., et al., 2013, *MNRAS*, **432**, 2696
 Naidu R. P., et al., 2022, *ApJ*, **940**, L14
 Oesch P. A., et al., 2013, *ApJ*, **773**, 75
 Oesch P. A., et al., 2014, *ApJ*, **786**, 108
 Oesch P. A., et al., 2016, *ApJ*, **819**, 129
 Oesch P. A., Bouwens R. J., Illingworth G. D., Labbé I., Stefanon M., 2018, *ApJ*, **855**, 105
 Oke J. B., 1974, *ApJS*, **27**, 21
 Oke J. B., Gunn J. E., 1983, *ApJ*, **266**, 713
 Paardekooper J.-P., Khochfar S., Dalla Vecchia C., 2015, *MNRAS*, **451**, 2544
 Robertson B. E., et al., 2022, *arXiv e-prints*, p. [arXiv:2212.04480](https://arxiv.org/abs/2212.04480)
 Salim S., Boquien M., Lee J. C., 2018, *ApJ*, **859**, 11
 Schmidt M., 1968, *ApJ*, **151**, 393
 Stark D. P., 2016, *ARA&A*, **54**, 761
 Tacchella S., Bose S., Conroy C., Eisenstein D. J., Johnson B. D., 2018, *ApJ*, **868**, 92
 Trenti M., Stiavelli M., 2008, *ApJ*, **676**, 767
 Wilkins S. M., et al., 2022, *MNRAS*,
 Williams C. C., et al., 2023, *arXiv e-prints*, p. [arXiv:2301.09780](https://arxiv.org/abs/2301.09780)
 Yung L. Y. A., Somerville R. S., Popping G., Finkelstein S. L., Ferguson H. C., Davé R., 2019, *MNRAS*, **490**, 2855

This paper has been typeset from a $\text{\TeX}/\text{\LaTeX}$ file prepared by the author.